Pair invariant mass to isolate background in the search for the chiral magnetic effect in Au + Au collisions at $\sqrt{s_{\mathrm{NN}}} = 200$ GeV

M. S. Abdallah,[5] J. Adam,[6] L. Adamczyk,[2] J. R. Adams,[39] J. K. Adkins,[30] G. Agakishiev,[28] I. Aggarwal,[41] M. M. Aggarwal,[41] Z. Ahammed,[60] I. Alekseev,[3,35] D. M. Anderson,[55] A. Aparin,[28] E. C. Aschenauer,[6] M. U. Ashraf,[11] F. G. Atetalla,[29] A. Attri,[41] G. S. Averichev,[28] V. Bairathi,[53] W. Baker,[10] J. G. Ball Cap,[20] K. Barish,[10] A. Behera,[52] R. Bellwied,[20] P. Bhagat,[27] A. Bhasin,[27] J. Bielcik,[14] J. Bielcikova,[38] I. G. Bordyuzhin,[3] J. D. Brandenburg,[6] A. V. Brandin,[35] I. Bunzarov,[28] J. Butterworth,[45] X. Z. Cai,[50] H. Caines,[63] M. Calderón de la Barca Sánchez,[8] D. Cebra,[8] I. Chakaberia,[31,6] P. Chaloupka,[14] B. K. Chan,[9] F-H. Chang,[37] Z. Chang,[6] N. Chankova-Bunzarova,[28] A. Chatterjee,[11] S. Chattopadhyay,[60] D. Chen,[10] J. Chen,[49] J. H. Chen,[18] X. Chen,[48] Z. Chen,[49] J. Cheng,[57] M. Chevalier,[10] S. Choudhury,[18] W. Christie,[6] X. Chu,[6] H. J. Crawford,[7] M. Csanád,[16] M. Daugherity,[1] T. G. Dedovich,[28] I. M. Deppner,[19] A. A. Derevschikov,[43] A. Dhamija,[41] L. Di Carlo,[62] L. Didenko,[6] X. Dong,[31] J. L. Drachenberg,[1] J. C. Dunlop,[6] N. Elsey,[62] J. Engelage,[7] G. Eppley,[45] S. Esumi,[58] O. Evdokimov,[12] A. Ewigleben,[32] O. Eyser,[6] R. Fatemi,[30] F. M. Fawzi,[5] S. Fazio,[6] P. Federic,[38] J. Fedorisin,[28] C. J. Feng,[37] Y. Feng,[44] P. Filip,[28] E. Finch,[51] Y. Fisyak,[6] A. Francisco,[63] C. Fu,[11] L. Fulek,[2] C. A. Gagliardi,[55] T. Galatyuk,[15] F. Geurts,[45] N. Ghimire,[54] A. Gibson,[59] K. Gopal,[23] X. Gou,[49] D. Grosnick,[59] A. Gupta,[27] W. Guryn,[6] A. I. Hamad,[29] A. Hamed,[5] Y. Han,[45] S. Harabasz,[15] M. D. Harasty,[8] J. W. Harris,[63] H. Harrison,[30] S. He,[11] W. He,[18] X. H. He,[26] Y. He,[49] S. Heppelmann,[8] S. Heppelmann,[42] N. Herrmann,[19] E. Hoffman,[20] L. Holub,[14] Y. Hu,[18] H. Huang,[37] H. Z. Huang,[9] S. L. Huang,[52] T. Huang,[37] X. Huang,[57] Y. Huang,[57] T. J. Humanic,[39] G. Igo,[9,*] D. Isenhower,[1] W. W. Jacobs,[25] C. Jena,[23] A. Jentsch,[6] Y. Ji,[31] J. Jia,[6,52] K. Jiang,[48] X. Ju,[48] E. G. Judd,[7] S. Kabana,[53] M. L. Kabir,[10] S. Kagamaster,[32] D. Kalinkin,[25,6] K. Kang,[57] D. Kapukchyan,[10] K. Kauder,[6] H. W. Ke,[6] D. Keane,[29] A. Kechechyan,[28] Y. V. Khyzhniak,[35] D. P. Kikoła,[61] C. Kim,[10] B. Kimelman,[8] D. Kincses,[16] I. Kisel,[17] A. Kiselev,[6] A. G. Knospe,[32] L. Kochenda,[35] L. K. Kosarzewski,[14] L. Kramarik,[14] P. Kravtsov,[35] L. Kumar,[41] S. Kumar,[26] R. Kunnawalkam Elayavalli,[63] J. H. Kwasizur,[25] S. Lan,[11] J. M. Landgraf,[6] J. Lauret,[6] A. Lebedev,[6] R. Lednicky,[28] J. H. Lee,[6] Y. H. Leung,[31] C. Li,[49] C. Li,[48] W. Li,[45] X. Li,[48] Y. Li,[57] X. Liang,[10] Y. Liang,[29] R. Licenik,[38] T. Lin,[55] Y. Lin,[11] M. A. Lisa,[39] F. Liu,[11] H. Liu,[25] H. Liu,[11] P. Liu,[52] T. Liu,[63] X. Liu,[39] Y. Liu,[55] Z. Liu,[48] T. Ljubicic,[6] W. J. Llope,[62] R. S. Longacre,[6] E. Loyd,[10] N. S. Lukow,[54] X. Luo,[11] L. Ma,[18] R. Ma,[6] Y. G. Ma,[18] N. Magdy,[12] R. Majka,[63,*] D. Mallick,[36] S. Margetis,[29] C. Markert,[56] H. S. Matis,[31] J. A. Mazer,[46] N. G. Minaev,[43] S. Mioduszewski,[55] B. Mohanty,[36] M. M. Mondal,[52] I. Mooney,[62] D. A. Morozov,[43] A. Mukherjee,[16] M. Nagy,[16] J. D. Nam,[54] Md. Nasim,[22] K. Nayak,[11] D. Neff,[9] J. M. Nelson,[7] D. B. Nemes,[63] M. Nie,[49] G. Nigmatkulov,[35] T. Niida,[58] R. Nishitani,[58] L. V. Nogach,[43] T. Nonaka,[58] A. S. Nunes,[6] G. Odyniec,[31] A. Ogawa,[6] S. Oh,[31] V. A. Okorokov,[35] B. S. Page,[6] R. Pak,[6] A. Pandav,[36] A. K. Pandey,[58] Y. Panebratsev,[28] P. Parfenov,[35] B. Pawlik,[40] D. Pawlowska,[61] H. Pei,[11] C. Perkins,[7] L. Pinsky,[20] R. L. Pintér,[16] J. Pluta,[61] B. R. Pokhrel,[54] G. Ponimatkin,[38] J. Porter,[31] M. Posik,[54] V. Prozorova,[14] N. K. Pruthi,[41] M. Przybycien,[2] J. Putschke,[62] H. Qiu,[26] A. Quintero,[54] C. Racz,[10] S. K. Radhakrishnan,[29] N. Raha,[62] R. L. Ray,[56] R. Reed,[32] H. G. Ritter,[31] M. Robotkova,[38] O. V. Rogachevskiy,[28] J. L. Romero,[8] L. Ruan,[6] J. Rusnak,[38] N. R. Sahoo,[49] H. Sako,[58] S. Salur,[46] J. Sandweiss,[63,*] S. Sato,[58] W. B. Schmidke,[6] N. Schmitz,[33] B. R. Schweid,[52] F. Seck,[15] J. Seger,[13] M. Sergeeva,[9] R. Seto,[10] P. Seyboth,[33] N. Shah,[24] E. Shahaliev,[28] P. V. Shanmuganathan,[6] M. Shao,[48] T. Shao,[50] A. I. Sheikh,[29] D. Shen,[50] S. S. Shi,[11] Y. Shi,[49] Q. Y. Shou,[18] E. P. Sichtermann,[31] R. Sikora,[2] M. Simko,[38] J. Singh,[41] S. Singha,[26] M. J. Skoby,[44] N. Smirnov,[63] Y. Söhngen,[19] W. Solyst,[25] P. Sorensen,[6] H. M. Spinka,[4,*] B. Srivastava,[44] T. D. S. Stanislaus,[59] M. Stefaniak,[61] D. J. Stewart,[63] M. Strikhanov,[35] B. Stringfellow,[44] A. A. P. Suaide,[47] M. Sumbera,[38] B. Summa,[42] X. M. Sun,[11] X. Sun,[12] Y. Sun,[48] Y. Sun,[21] B. Surrow,[54] D. N. Svirida,[3] Z. W. Sweger,[8] P. Szymanski,[61] A. H. Tang,[6] Z. Tang,[48] A. Taranenko,[35] T. Tarnowsky,[34] J. H. Thomas,[31] A. R. Timmins,[20] D. Tlusty,[13] T. Todoroki,[58] M. Tokarev,[28] C. A. Tomkiel,[32] S. Trentalange,[9] R. E. Tribble,[55] P. Tribedy,[6] S. K. Tripathy,[16] T. Truhlar,[14] B. A. Trzeciak,[14] O. D. Tsai,[9] Z. Tu,[6] T. Ullrich,[6] D. G. Underwood,[4] I. Upsal,[49,6] G. Van Buren,[6] J. Vanek,[38] A. N. Vasiliev,[43] I. Vassiliev,[17] V. Verkest,[62] F. Videbæk,[6] S. Vokal,[28] S. A. Voloshin,[62] F. Wang,[44] G. Wang,[9] J. S. Wang,[21] P. Wang,[48] Y. Wang,[11] Y. Wang,[57] Z. Wang,[49] J. C. Webb,[6] P. C. Weidenkaff,[19] L. Wen,[9] G. D. Westfall,[34] H. Wieman,[31] S. W. Wissink,[25] J. Wu,[26] Y. Wu,[10] B. Xi,[50] Z. G. Xiao,[57] G. Xie,[31] W. Xie,[44] H. Xu,[21] N. Xu,[31] Q. H. Xu,[49] Y. Xu,[49] Z. Xu,[6] Z. Xu,[9] C. Yang,[49] Q. Yang,[49] S. Yang,[45] Y. Yang,[37] Z. Ye,[45] Z. Ye,[12] L. Yi,[49] K. Yip,[6] Y. Yu,[49] H. Zbroszczyk,[61] W. Zha,[48] C. Zhang,[52] D. Zhang,[11] J. Zhang,[49] S. Zhang,[12] S. Zhang,[18] X. P. Zhang,[57] Y. Zhang,[26] Y. Zhang,[48] Y. Zhang,[11] Z. J. Zhang,[37] Z. Zhang,[6] Z. Zhang,[12] J. Zhao,[18] C. Zhou,[18] X. Zhu,[57] Z. Zhu,[49] M. Zurek,[31] and M. Zyzak[17]

(STAR Collaboration)

[1]*Abilene Christian University, Abilene, Texas 79699*
[2]*AGH University of Science and Technology, FPACS, Cracow 30-059, Poland*
[3]*Alikhanov Institute for Theoretical and Experimental Physics NRC "Kurchatov Institute", Moscow 117218*
[4]*Argonne National Laboratory, Argonne, Illinois 60439*
[5]*American University of Cairo, New Cairo 11835, New Cairo, Egypt*

*Deceased.

[6]*Brookhaven National Laboratory, Upton, New York 11973*

[7]*University of California, Berkeley, California 94720*

[8]*University of California, Davis, California 95616*

[9]*University of California, Los Angeles, California 90095*

[10]*University of California, Riverside, California 92521*

[11]*Central China Normal University, Wuhan, Hubei 430079*

[12]*University of Illinois at Chicago, Chicago, Illinois 60607*

[13]*Creighton University, Omaha, Nebraska 68178*

[14]*Czech Technical University in Prague, FNSPE, Prague 115 19, Czech Republic*

[15]*Technische Universität Darmstadt, Darmstadt 64289, Germany*

[16]*ELTE Eötvös Loránd University, Budapest H-1117, Hungary*

[17]*Frankfurt Institute for Advanced Studies FIAS, Frankfurt 60438, Germany*

[18]*Fudan University, Shanghai 200433*

[19]*University of Heidelberg, Heidelberg 69120, Germany*

[20]*University of Houston, Houston, Texas 77204*

[21]*Huzhou University, Huzhou, Zhejiang 313000*

[22]*Indian Institute of Science Education and Research (IISER),
Berhampur 760010, India*

[23]*Indian Institute of Science Education and Research (IISER) Tirupati,
Tirupati 517507, India*

[24]*Indian Institute Technology, Patna, Bihar 801106, India*

[25]*Indiana University, Bloomington, Indiana 47408*

[26]*Institute of Modern Physics, Chinese Academy of Sciences, Lanzhou,
Gansu 730000*

[27]*University of Jammu, Jammu 180001, India*

[28]*Joint Institute for Nuclear Research, Dubna 141 980*

[29]*Kent State University, Kent, Ohio 44242*

[30]*University of Kentucky, Lexington, Kentucky 40506-0055*

[31]*Lawrence Berkeley National Laboratory, Berkeley, California 94720*

[32]*Lehigh University, Bethlehem, Pennsylvania 18015*

[33]*Max-Planck-Institut für Physik, Munich 80805, Germany*

[34]*Michigan State University, East Lansing, Michigan 48824*

[35]*National Research Nuclear University MEPhI, Moscow 115409*

[36]*National Institute of Science Education and Research, HBNI, Jatni 752050, India*

[37]*National Cheng Kung University, Tainan 70101*

[38]*Nuclear Physics Institute of the CAS, Rez 250 68, Czech Republic*

[39]*Ohio State University, Columbus, Ohio 43210*

[40]*Institute of Nuclear Physics PAN, Cracow 31-342, Poland*

[41]*Panjab University, Chandigarh 160014, India*

[42]*Pennsylvania State University, University Park, Pennsylvania 16802*

[43]*NRC "Kurchatov Institute", Institute of High Energy Physics,
Protvino 142281*

[44]*Purdue University, West Lafayette, Indiana 47907*

[45]*Rice University, Houston, Texas 77251*

[46]*Rutgers University, Piscataway, New Jersey 08854*

[47]*Universidade de São Paulo, São Paulo 05314-970, Brazil*

[48]*University of Science and Technology of China, Hefei, Anhui 230026*

[49]*Shandong University, Qingdao, Shandong 266237*

[50]*Shanghai Institute of Applied Physics, Chinese Academy of Sciences, Shanghai 201800*

[51]*Southern Connecticut State University, New Haven, Connecticut 06515*

[52]*State University of New York, Stony Brook, New York 11794*

[53]*Instituto de Alta Investigación, Universidad de Tarapacá, Arica 1000000, Chile*

[54]*Temple University, Philadelphia, Pennsylvania 19122*

[55]*Texas A&M University, College Station, Texas 77843*

[56]*University of Texas, Austin, Texas 78712*

[57]*Tsinghua University, Beijing 100084*

[58]*University of Tsukuba, Tsukuba, Ibaraki 305-8571, Japan*

[59]*Valparaiso University, Valparaiso, Indiana 46383*

[60]*Variable Energy Cyclotron Centre, Kolkata 700064, India*

[61]*Warsaw University of Technology, Warsaw 00-661, Poland*
[62]*Wayne State University, Detroit, Michigan 48201*
[63]*Yale University, New Haven, Connecticut 06520*

Quark interactions with topological gluon configurations can induce local chirality imbalance and parity violation in quantum chromodynamics, which can lead to the chiral magnetic effect (CME)—an electric charge separation along the strong magnetic field in relativistic heavy-ion collisions. The CME-sensitive azimuthal correlator observable ($\Delta\gamma$) is contaminated by background arising, in part, from resonance decays coupled with elliptic anisotropy (v_2). We report here differential measurements of the correlator as a function of the pair invariant mass ($m_{\rm inv}$) in 20–50% centrality Au + Au collisions at $\sqrt{s_{\rm NN}} = 200$ GeV by the STAR experiment at the BNL Relativistic Heavy Ion Collider. Strong resonance background contributions to $\Delta\gamma$ are observed. At large $m_{\rm inv}$ where this background is significantly reduced, the $\Delta\gamma$ value is found to be significantly smaller. An event-shape-engineering technique is deployed to determine the v_2 background shape as a function of $m_{\rm inv}$. We extract a v_2-independent and $m_{\rm inv}$-averaged signal $\Delta\gamma_{\rm sig} = (0.03 \pm 0.06 \pm 0.08) \times 10^{-4}$, or $(2 \pm 4 \pm 5)\%$ of the inclusive $\Delta\gamma (m_{\rm inv} > 0.4~{\rm GeV}/c^2) = (1.58 \pm 0.02 \pm 0.02) \times 10^{-4}$, within pion $p_T = 0.2$–0.8 GeV/c and averaged over pseudorapidity ranges of $-1 < \eta < -0.05$ and $0.05 < \eta < 1$. This represents an upper limit of 0.23×10^{-4}, or 15% of the inclusive result, at 95% confidence level for the $m_{\rm inv}$-integrated CME contribution.

I. INTRODUCTION

Quark interactions with topological gluon fields can induce chirality imbalance and local parity violation in quantum chromodynamics (QCD) [1–3]. This can lead to electric charge separation in the presence of a strong magnetic field, a phenomenon known as the chiral magnetic effect (CME) [4,5]. Such a strong magnetic field is likely present in noncentral heavy-ion collisions, mainly generated by the spectator protons [6,7], and may last an extended period of time [8,9]. It has been suggested that the CME correlation signal can be observable in heavy-ion collisions [10,11] at the BNL Relativistic Heavy-Ion Collider (RHIC) and the CERN Large Hadron Collider (LHC) [3,6]. Extensive efforts have been devoted to the search for a CME-induced charge separation along the magnetic field in heavy-ion collisions (see reviews in Refs. [12–16]). Many analysis techniques are being pursued [17–20], and a CME-motivated isobar collision program was conducted at the RHIC in 2018 [21,22].

In noncentral, i.e., finite impact parameter (b), heavy-ion collisions, the magnetic field is, on average, perpendicular to the reaction plane (defined by the impact parameter direction and the beam). A surrogate for the reaction plane is the participant plane [23], which, in turn, can be estimated using the second-order harmonic plane (ψ_2) from the azimuthal distribution of final-state particles. Because topological fluctuations are random, the single-particle asymmetry resulting from the charge separation vanishes. One needs to resort to two-particle correlations, a common observable of which is the three-point correlator with respect to ψ_2 [24]:

$$\gamma \equiv \langle \cos(\phi_\alpha + \phi_\beta - 2\psi_2) \rangle, \qquad (1)$$

where ϕ_α and ϕ_β are the azimuthal angles of particles α and β, respectively, either of same-sign (SS) or opposite-sign (OS) electric charges. The CME would result in SS pairs close in

azimuth and OS pairs back-to-back, both perpendicular to ψ_2, yielding $\gamma_{\rm SS} = -1$ and $\gamma_{\rm OS} = +1$.

It has been argued, prompted by data measurements [25,26], that it is possible that the OS pair correlations are lost because of medium interactions and some of the SS pairs can still survive [6]. On the other hand, the underlying event could have charge-independent and charge-dependent correlations from non-CME physics. These backgrounds can also alter the OS and SS correlations in such a way that they are not symmetric about zero any more. To remove the charge-independent background (e.g., from global momentum conservation), the correlator difference,

$$\Delta\gamma \equiv \gamma_{\rm OS} - \gamma_{\rm SS}, \qquad (2)$$

is used [24]. A CME signal would yield a measurement of $\Delta\gamma > 0$, the magnitude of which would be diluted by non-CME pairs. However, charge-dependent background correlations also exist, such as those from resonance decays [24,27]. This is illustrated schematically in Fig. 1 using $\rho \to \pi^+\pi^-$ as an example, where the gray plane indicates the reaction plane and the total orbital angular momentum and the magnetic field are, on average, perpendicular to the reaction plane. Because more particles/resonances are produced parallel to ψ_2 than perpendicular to ψ_2, as quantified by the elliptic flow anisotropy parameter $v_{2,{\rm res}}$, the overall effect is a positive background, $\Delta\gamma_{\rm bkgd} > 0$. This flow-induced background can be expressed as $\Delta\gamma_{\rm bkgd} \propto \langle \cos(\phi_\alpha + \phi_\beta - 2\phi_{\rm res}) \rangle v_{2,{\rm res}}$, where $\phi_{\rm res}$ is the resonance azimuth, and α and β are the resonance decay daughters [15,24,27–29].

Positive $\Delta\gamma$ is indeed observed at the level of $\sim 10^{-4}$ in midcentral heavy-ion collisions where the two nuclei partially overlap at intermediate b values [25,26,31–33]. A difficulty in its CME interpretation is the large charge-dependent background aforementioned, the magnitude of which dominates or may even fully account for the measured $\Delta\gamma$ [7,15,17,28,33–38]. The first experimental demonstration of
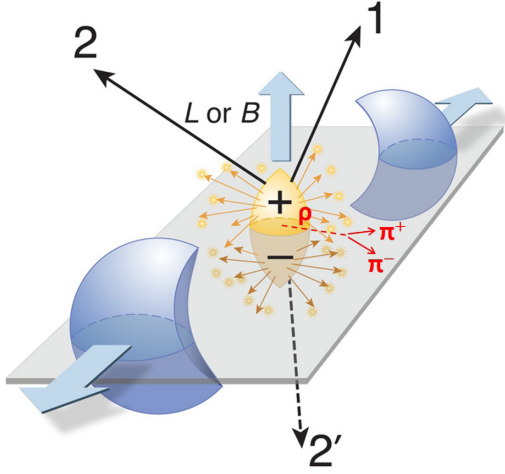
FIG. 1. Schematic view of the charge separation along the system orbital momentum ($\vec{L}$), which coincides with the magnetic field ($\vec{B}$) direction. The arrows 1 and 2 represent a SS pair close in azimuth, and 1 and 2′ represent a OS pair "back-to-back." The ρ resonance at ψ_2 decays into a $\pi^+\pi^-$ pair, giving a positive $\Delta\gamma_{OS}$. This illustration is based on a figure in Ref. [30].

such a background comes from proton-lead collisions, where the participant plane is determined purely by geometry fluctuations (e.g., the proton strikes several nucleons in the lead nucleus, giving an irregular overlap shape), essentially uncorrelated with the impact parameter or the magnetic field direction [33]. Any CME signal is expected to be negligible in small systems, and yet, a large $\Delta\gamma$ value was observed in $p +$ Pb collisions at the LHC, similar to that in Pb + Pb collisions. This challenged the CME interpretation of the heavy-ion data [33]. A large $\Delta\gamma$ is also observed in $p(d) +$ Au collisions at the RHIC [39]. Event-shape engineering (ESE) [40], where events are selected within the same centrality bin but differing in v_2, has been used at the LHC to derive upper limits on the CME [17,18]. The CME signal likely depends on the collision energy, but quantitative predictions are difficult [6,11,41,42]. To date, no quantitative conclusion on the CME has been reached at the RHIC; an upper limit, as we report here, should provide significant insights into the CME at the RHIC.

In order to isolate the resonance background contributions, we report measurements of the $\Delta\gamma$ variable, differential in pair invariant mass (m_{inv}). The integral $\Delta\gamma$ with a minimum m_{inv} limit is presented. To fully exploit the data, an ESE [40] technique is deployed to determine the v_2 background shape as a function of m_{inv}. The $\Delta\gamma(m_{\text{inv}})$ data are then fitted to the v_2 background shape plus an m_{inv}-independent constant term. The extracted constant term represents a v_2-independent component in the data, possibly an m_{inv}-integrated CME signal.

II. EXPERIMENT AND DATA ANALYSIS

The data reported here were taken by the STAR experiment at the center-of-mass energy per nucleon pair of $\sqrt{s_{NN}} = 200$ GeV in the years 2011, 2014, and 2016. A total of 2.5×10^9 minimum-bias (MB) triggered events were used in the analysis. The STAR apparatus is described in Ref. [43].

The main detectors used in this analysis are the time projection chamber (TPC) [44,45] and the time-of-flight (TOF) detector [46]. Track trajectories are reconstructed from hits detected in the TPC; at least 10 points out of a possible maximum of 45 points are required for a valid track. The primary interaction vertex is reconstructed from those tracks. Events with primary vertices within 30 cm (year 2011) or 6 cm (years 2014 and 2016) longitudinally and within 2 cm in the transverse plane from the geometrical center of the TPC are used. The event centrality is determined from the multiplicity of those charged particle tracks which are within pseudorapidity $|\eta| < 0.5$ and have a distance of closest approach (DCA) to the primary vertex of less than 3 cm.

Tracks used for the analysis are required to have at least 20 points used in track fitting, and a DCA of less than 1 cm. The fraction of fit points out of the maximum allowed by the TPC geometry is required to be greater than 0.52 to avoid track splitting. Particle momenta are determined by the track trajectories in the STAR magnetic field. A minimum transverse momentum ($p_T > 0.2$ GeV/c) is required to ensure that each track traversing the TPC can reach the TOF detector. The charged particles can be identified by their ionization energy loss (dE/dx) in the TPC gas and their time of flight from the TOF detector. Pions are identified up to $p_T = 0.8$ GeV/c with dE/dx and extended to $p_T = 1.8$ GeV/c with the TOF.

This analysis uses the three-particle correlator:

$$\gamma = \langle\cos(\phi_\alpha + \phi_\beta - 2\phi_c)\rangle/v_{2,c}, \qquad (3)$$

where α and β represent the pion index, and the average $\langle\cdots\rangle$ runs over all triplets and over all events. The azimuthal angle of the third particle, ϕ_c, serves as a measure of ψ_2. The imprecision in determining the ψ_2 by a single particle is corrected by the resolution factor, equal to the particle's elliptic flow anisotropy $v_{2,c}$. Charged TPC tracks with p_T from 0.2 to 2 GeV/c are used for particle c. Two methods are used: (i) the subevent method, the main method used in this analysis, where the α and β particles are from one half of the TPC ($-1 < \eta < -0.05$ or $0.05 < \eta < 1$) and the particle c is from the other half ($0.05 < \eta < 1$ or $-1 < \eta < -0.05$) [47]; and (ii) the full-event method, where the α, β, and c particles are all taken from the pseudorapidity range $|\eta| < 1$ [25,26]. The η gap of 0.1 between the positive and negative pseudorapidity subevents is to suppress short-range correlations from quantum interference and Coulomb interaction, as well as detector-related effects such as track splitting [22]. In order to identify resonance decay contributions, the $\Delta\gamma$ correlator is studied as a function of m_{inv} of the α and β particle pairs. The analysis loops over α and β particles, and the c particle is handled by the cumulant method [48].

The systematic uncertainties are estimated for each run by varying the required minimum number of hit points from 20 to 15, and the DCA from 1.0 cm to 2.0 and 0.8 cm. In the full-event method, the η gap used to determine $v_{2,c}$ via two-particle correlations is varied from 1 to 0.5 and 1.4 [39,47]. In the subevent method, the η gap between the two subevents is varied from 0.1 to 0.3 [49]. For each variation, the statistical fluctuation effect arising from the change in the data sample is subtracted. For each source when multiple variations are assessed, the systematic uncertainty is taken as the root mean

TABLE I. The absolute systematic uncertainties on the extracted possible CME signal fraction (as a percentage) in the inclusive $\Delta\gamma$ in $20-50\%$ centrality Au + Au collisions at 200 GeV from the ESE fit method.

DCA	Number of points	Subevent η gap	Total
$\pm 2\%$	$\pm 3\%$	$\pm 3\%$	$\pm 5\%$

square. The systematic uncertainties from the above sources are added in quadrature for each dataset of the three runs. The three datasets are then combined assuming their systematic uncertainties are fully correlated.

The pion purity in this analysis is approximately 98%; the systematic uncertainty from particle identification is found to be negligible. The effect of different charge combinations among the three particles in Eq. (3) has been studied in Ref. [25] and found to cause negligible difference in the $\Delta\gamma$ results.

For the extracted possible CME signal from the ESE fit method, a fit result is obtained for each of the above variations, and the systematic uncertainty is estimated in the same way as described above. The estimated absolute systematic uncertainties on the extracted CME signal fraction in the $20-50\%$ centrality are 2%, 3%, and 3% for the DCA, the number of hit points, and the η gap variations, respectively. The m_{inv} range used in the ESE fit is varied from above 0.4 GeV/c^2 to above 0.35 and 0.45 GeV/c^2, which yields negligible change in the results. Table I summarizes the systematic uncertainties on the extracted possible CME signal fraction.

III. RESULTS AND DISCUSSIONS

A. $\Delta\gamma$ as a function of m_{inv}

Figure 2(a) shows the number of OS and SS $\pi^+\pi^-$ pairs as functions of m_{inv} for $20-50\%$ centrality Au + Au collisions at $\sqrt{s_{NN}} = 200$ GeV. Pions are identified by the TPC dE/dx method within $0.2 < p_T < 0.8$ GeV/c. The subevent method is used. The N_{OS} and N_{SS} are nearly identical. Figure 2(b) shows the average correlators for OS and SS pairs, γ_{OS} and γ_{SS}, respectively. The positive (negative) values at low (high) m_{inv} arise from pair kinematics coupled with particle v_2. Low-m_{inv} pairs tend to be close in azimuth and hence lead to positive γ values, while high-m_{inv} pairs tend to be back-to-back and hence lead to negative γ values. Because of these correlations between m_{inv} and the pair opening angle, γ_{OS} and γ_{SS} vary over a large range as a function of m_{inv} and look nearly identical. The integrated γ_{OS} and γ_{SS} (of pions in this analysis) over m_{inv} (effectively over the opening angle) are close to zero and comparable with previous results of charged hadrons [25,26]. These kinematics-related large variations in γ_{OS} and γ_{SS} over m_{inv} are removed in the difference of Eq. (2), which we present next.

Figure 3(a) shows the relative OS and SS $\pi^+\pi^-$ pair abundance difference, $r = (N_{OS} - N_{SS})/N_{OS}$, as a function of m_{inv} for $20-50\%$ centrality Au + Au collisions at $\sqrt{s_{NN}} = 200$ GeV. Figure 3(b) shows the measured $\Delta\gamma$ as a function
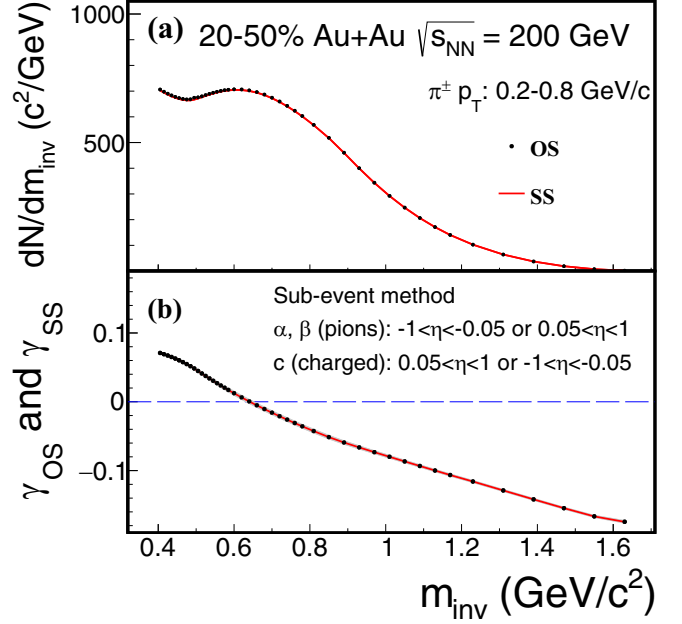

FIG. 2. The m_{inv} dependencies of (a) the OS and SS pion pair multiplicities and (b) γ_{OS} and γ_{SS} in $20-50\%$ Au + Au collisions at 200 GeV. Error bars are statistical. The shaded areas in panel (b) are systematic uncertainties, which are small.

of m_{inv} in a similar way. The $m_{inv} < 0.4$ GeV/c^2 region is excluded because the acceptance difference between OS and SS pairs, mostly close in azimuthal angle, becomes unreasonably large. This is due to the charge-dependent nonuniformity of the TPC acceptance/efficiency in the azimuthal direction;
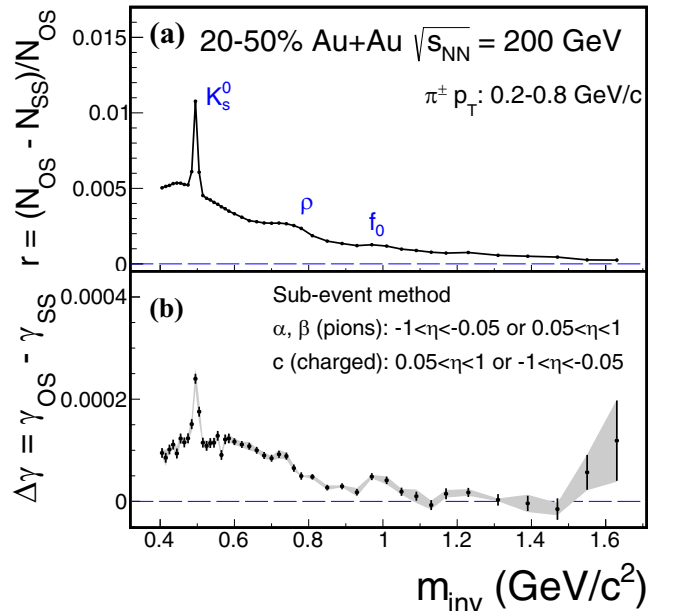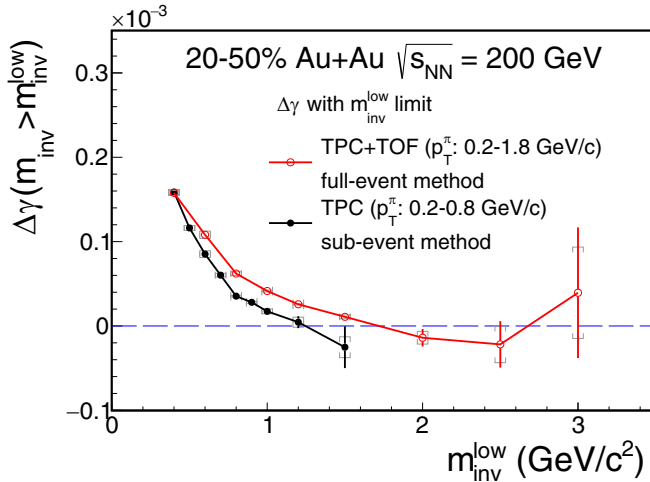

FIG. 3. m_{inv} dependencies of (a) the relative excess of OS over SS pion pairs and (b) $\Delta\gamma = \gamma_{OS} - \gamma_{SS}$ in $20-50\%$ Au + Au collisions at 200 GeV. Error bars are statistical. The shaded areas in panel (b) are systematic uncertainties.

FIG. 4. The π pair $\Delta\gamma$ at $m_{\mathrm{inv}} > m_{\mathrm{inv}}^{\mathrm{low}}$ for the data shown in Fig. 3 identified by the TPC (black points) and for the more extended p_T range identified by the TPC and TOF (red circles). Error bars are statistical. The caps are systematic uncertainties.

the correction becomes too large at small m_{inv}. As shown in Fig. 3(b), a clear peak from $K_s^0 \rightarrow \pi^+ + \pi^-$ decay is observed in $\Delta\gamma$, and possible ρ^0 and f_0 peaks are also visible [50]. These peaks correspond to the resonance production peaks in r shown in Fig. 3(a). The results indicate strong contributions from resonances to the $\Delta\gamma$ observable.

It is clear from the comparison of the two panels in Fig. 3 that the inclusive $\Delta\gamma$ measurement is contaminated by a large background caused by resonance decays and correlated particle pairs. The possible CME signal is, in principle, hidden within the large background in the $\Delta\gamma$ measurement of Fig. 3(b). This CME signal would be the difference in γ_{OS} and γ_{SS} inherited from initial correlations, rather than correlations from the final state, such as resonance decays.

B. $\Delta\gamma$ at large m_{inv}

As indicated by Fig. 3(a), most of the excess of OS over SS pion pairs is from the small m_{inv} region (approximately 96% at $m_{\mathrm{inv}} < 1 \text{ GeV}/c^2$). Applying a minimum m_{inv} requirement would reduce those contributions. On the other hand, a lower m_{inv} cut would remove a large fraction of low-p_T pions. It may thus reduce the possible CME signal because the CME is theoretically conjectured to be a low-p_T phenomenon [6,25]. A recent study [11], however, suggests a rather p_T-independent signal above 0.2 GeV/c.

In any case, it is interesting to examine the $\Delta\gamma(m_{\mathrm{inv}} > m_{\mathrm{inv}}^{\mathrm{low}})$ above a certain $m_{\mathrm{inv}}^{\mathrm{low}}$ value, which would be more sensitive to the CME signal if the signal is a more slowly decreasing function of m_{inv} than resonance contributions. This is presented in Fig. 4, where two results are shown. Black points show $\Delta\gamma(m_{\mathrm{inv}} > m_{\mathrm{inv}}^{\mathrm{low}})$ for data in Fig. 3. Because the pions are identified by the TPC up to $p_T = 0.8$ GeV/c, the data do not reach a large enough m_{inv}. In order to measure the spectra at large m_{inv} with high statistics, we include the pions identified by TPC and TOF detectors with p_T extended to 1.8 GeV/c, and the full-event method is used. The
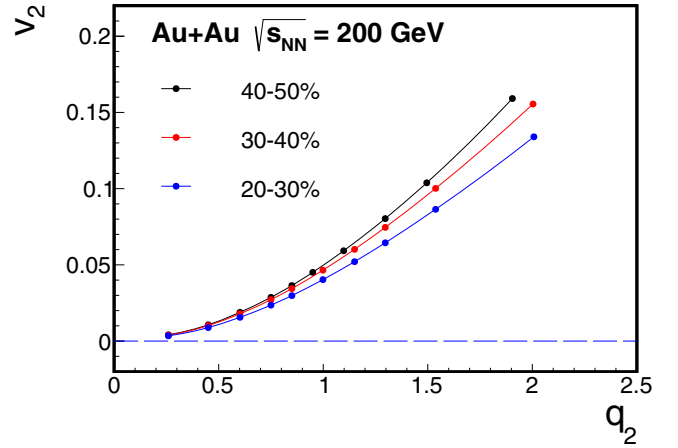

FIG. 5. The elliptic flow v_2 in bins of q_2 for the three centrality bins in the $20-50\%$ range of Au + Au collisions at 200 GeV.

result is shown in red circles. The result from the full-event method with the higher p_T range is systematically larger than that from the subevent method with the limited p_T range. The reasons are twofold: $\Delta\gamma$ has been found to increase with p_T [25] and the η gap in the subevent method suppresses the correlation background. For both cases, $\Delta\gamma(m_{\mathrm{inv}} > m_{\mathrm{inv}}^{\mathrm{low}})$ decreases with increasing $m_{\mathrm{inv}}^{\mathrm{low}}$ and approaches zero when $m_{\mathrm{inv}}^{\mathrm{low}}$ becomes large. Note that residual resonance and other correlation backgrounds may still remain at high mass, and detailed model and theoretical studies are required to draw further conclusions.

C. Event-shape engineering to extract CME

In order to fully exploit the data to extract a possible CME signal over the entire m_{inv} range, resonance contributions need to be removed. This may be achieved by taking advantage of the presumably different m_{inv} dependencies of the background and the possible CME signal. Assuming the $\Delta\gamma$ data contain the flow-induced background and a possible CME signal, the inclusive $\Delta\gamma$ can be expressed as [51]

$$\Delta\gamma(m_{\mathrm{inv}}) = r(m_{\mathrm{inv}})\langle\cos(\phi_\alpha + \phi_\beta - 2\phi_{\mathrm{res}})\rangle v_{2,\mathrm{res}} + \Delta\gamma_{\mathrm{sig}}.$$

(4)

The first term of the right-hand side of Eq. (4) is the background and is obviously dependent on m_{inv} and v_2. The second term is the possible CME signal.

We attempt to separate the background and the CME by resorting to the ESE method. The ESE method selects events from a narrow centrality bin with different v_2 values by using the reduced flow vector q_2 quantity; $q_2 = |\sum_{j=1}^{N} e^{i2\phi_j}|/\sqrt{N}$ summing over the α and β particles in each event using the subevent method. The v_2 value is calculated as a function of q_2 by the correlations with respect to the particles from the other subevent. Figure 5 shows the v_2 values in bins of q_2 in each narrow centrality bin. The v_2 value is strongly correlated with q_2 because the α and β particles are used for both the q_2 and v_2 calculations. In other words, this ESE method is selecting mainly on the statistical fluctuations of the α/β particle's elliptic anisotropy, which has a wide spread. The v_2 value does
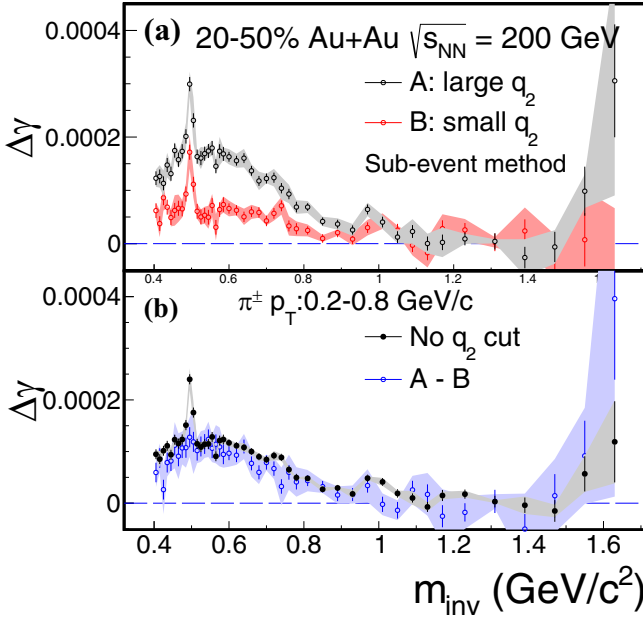
FIG. 6. m_{inv} dependencies of (a) the $\Delta\gamma$ values from ESE-selected event samples A (50% largest q_2) and B (50% smallest q_2), respectively, and (b) the inclusive (no q_2 restriction) $\Delta\gamma$ compared with $\Delta\gamma_A - \Delta\gamma_B$ in $20-50\%$ Au + Au collisions at 200 GeV. Error bars are statistical. The shaded areas are systematic uncertainties.

not linearly depend on q_2, especially at small values of q_2. This has also been observed in simulations [52].

The events shown in Fig. 3 are divided into two equal-size groups according to the q_2 value in each narrow centrality bin: event sample A with the 50% largest q_2 and event sample B with the 50% smallest q_2, as indicated in Fig. 5(a). The q_2 cut values to separate events are similar among the three centrality bins. The $\Delta\gamma$ values are calculated in the two halves of events for each centrality bin and then are combined. Figure 6(a) shows the m_{inv} dependence of the $\Delta\gamma_A$ and $\Delta\gamma_B$ from event samples A and B, respectively, integrated over the $20-50\%$ centrality range. Figure 6(b) shows the inclusive [no q_2 restriction, i.e., the same data as shown in Fig. 3(b)] $\Delta\gamma$ compared with $\Delta\gamma_A - \Delta\gamma_B$. The systematic uncertainty of the latter is larger than twice that of the former, which is approximately $(\Delta\gamma_A + \Delta\gamma_B)/2$. This is due to an anticorrelation between the two event classes as they are selected largely on statistical fluctuations as aforementioned.

In order to exploit the presumably different m_{inv} dependencies of the background and the signal to extract the CME, we need to assess the background shape in m_{inv}. To this end, we first have verified that the $r(m_{inv})$ distributions are the same between the two event classes. The decay angular correlations, $\langle\cos(\phi_\alpha + \phi_\beta - 2\phi_{res})\rangle$, are presumably also the same. It is probably safe to assume that $v_2(m_{inv})$ has the same m_{inv} dependence for the different q_2 event classes, only differing in magnitude. Under this assumption, the backgrounds in different q_2 event classes will have the same shape in m_{inv}, differing only in its overall magnitude. The CME depends on the overall magnetic field. As mentioned in the Introduction, the magnetic field is primarily produced by spectator
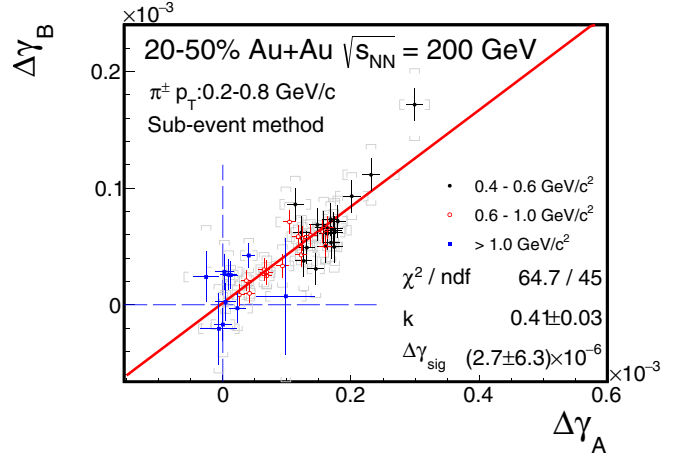

FIG. 7. $\Delta\gamma_A$ versus $\Delta\gamma_B$ in $20-50\%$ Au + Au collisions at 200 GeV, with the linear function fit of Eq. (5). Error bars are statistical. Horizontal and vertical caps are the systematic uncertainties on $\Delta\gamma_A$ and $\Delta\gamma_B$. Marker colors indicate the data from different m_{inv} regions (black: 0.4–0.6 GeV/c^2; red: 0.6–1.0 GeV/c^2; blue: >1.0 GeV/c^2).

protons. Because the spectator protons and the participant particle anisotropy are uncorrelated [19], the CME is largely independent of the v_2 of the different q_2 classes. However, the participant protons do contribute to the overall magnetic field [53–55]. Model calculations indicate that such a contribution could account for 20% of the overall magnetic field strength in Au + Au collisions of medium centrality [55]. This magnetic field contribution could have variations over the different q_2 event classes due to the presumably different event shape selected by q_2. In this paper, we assume such variation is small and proceed with the assumption that the CME is independent of q_2 and v_2 Then the difference of the $\Delta\gamma(m_{inv})$ from the different q_2 event classes can be regarded as the background $\Delta\gamma_{bkgd}(m_{inv})$ shape [13].

The inclusive $\Delta\gamma$ contains both the background and the possible CME. We further assume that the possible CME signal is independent of m_{inv}. Then, with the background shape given by $\Delta\gamma_A - \Delta\gamma_B$, the possible CME signal can be extracted from a two-parameter fit: $\Delta\gamma = b(\Delta\gamma_A - \Delta\gamma_B) + \Delta\gamma_{sig}$. However, because the same data are used in $\Delta\gamma$ and $\Delta\gamma_A - \Delta\gamma_B$, their statistical errors are not independent. To properly handle statistical errors, an alternative function is used to fit the two independent measurements of $\Delta\gamma_A$ versus $\Delta\gamma_B$, namely,

$$\Delta\gamma_B = k\Delta\gamma_A + (1-k)\Delta\gamma_{sig}, \qquad (5)$$

where k and $\Delta\gamma_{sig}$ are the fit parameters. Because $\Delta\gamma \approx (\Delta\gamma_A + \Delta\gamma_B)/2$, then $b \approx (1+k)/(1-k)/2$. In this fit model, the background is not required to be strictly proportional to v_2, but only dependent on v_2 [51,56].

Figure 7 shows $\Delta\gamma_A$ versus $\Delta\gamma_B$ in $20-50\%$ centrality Au + Au collisions at 200 GeV. Each data point corresponds to one m_{inv} bin in Fig. 7(a). The line is the fit by Eq. (5). The fitted $\Delta\gamma_{sig}$ is $(0.03 \pm 0.06 \pm 0.08) \times 10^{-4}$ and is found to be $(2 \pm 4 \pm 5)\%$ of the inclusive $\Delta\gamma(m_{inv} > 0.4$ GeV/$c^2) =$

$(1.58 \pm 0.02 \pm 0.02) \times 10^{-4}$. These values represent over an order of magnitude reduction from the inclusive $\Delta\gamma$ measurement. Our results indicate that the possible CME signal is small in the inclusive $\Delta\gamma$, consistent with zero with current precision. This presents an upper limit of 0.23×10^{-4}, or 15% of the inclusive result at the 95% confidence level [57].

We note, as previously discussed, that our two-component fit model is based on the following assumptions: (i) the $v_2(m_{\text{inv}})$ dependence is the same between the two q_2 event classes, (ii) the magnetic field contribution from participant protons has negligible variation between the two q_2 event classes, and (iii) the CME signal $\Delta\gamma_{\text{sig}}$ is independent of m_{inv}. The χ^2/ndf of our fit in Fig. 7 indicates a p value of 2.86%, which suggests that our assumptions may be reasonable, but future improvement with the help of theoretical calculations is possible. Nevertheless, the fitted $\Delta\gamma_{\text{sig}}$ may be interpreted as the signal averaged over the m_{inv} range. The potential CME could depend on m_{inv}, and given enough statistics, such details could be investigated experimentally by more sophisticated ESE analysis.

Our result is consistent with our previous finding from an ESE analysis [37] and a more recent measurement using spectator and participant planes [58]. The recent isobar data [22] do not yield an observable CME signal, in line with the present work. Our upper limit is quantitatively similar to those reported at the LHC [17,18]. Quantitative predictions of the CME signal strength are not available at the RHIC or the LHC; only a general expectation of 10^{-4} has been suggested [10,11]. Our upper limit, together with those at the LHC, add significant insights to the physics of the CME and calls for further theoretical inputs.

IV. CONCLUSIONS

In summary, we report differential measurements of the reaction-plane-dependent azimuthal correlation of pion pairs ($\Delta\gamma$), sensitive to the topological-charge-induced chiral magnetic effect in QCD, as a function of the pair invariant mass (m_{inv}). Resonance structures are observed in $\Delta\gamma(m_{\text{inv}})$, indicating the dominance of background contributions in the previous inclusive $\Delta\gamma$ measurements [25,26,31]. At large m_{inv}, where this background is significantly reduced, the $\Delta\gamma$ is also significantly smaller. To isolate the possible CME signal from the background, event-shape engineering

by the subevent method is used to determine the background shape in m_{inv}. The background shape is used in a two-component fit to the $\Delta\gamma(m_{\text{inv}})$ data, assuming it contains a v_2-independent signal in additional to the v_2-dependent background. Such a fit yields a v_2-independent signal of $\Delta\gamma_{\text{sig}} = (0.03 \pm 0.06 \pm 0.08) \times 10^{-4}$ in 20−50% centrality Au + Au collisions at 200 GeV, $(2 \pm 4 \pm 5)$% of the inclusive measurement of $\Delta\gamma(m_{\text{inv}} > 0.4 \text{ GeV}/c^2) = (1.58 \pm 0.02 \pm 0.02) \times 10^{-4}$, within pion $p_{\text{T}} = 0.2$–0.8 GeV/c and averaged between pseudorapidity ranges of $-1 < \eta < -0.05$ and $0.05 < \eta < 1$. This represents an upper limit of 0.23×10^{-4}, or 15% of the inclusive result, at the 95% confidence level for the possible CME signal integrated over m_{inv}. This constitutes a report of an upper limit on the theoretically predicted CME at the RHIC, with explicit isolation of background and under several assumptions. Theoretical inputs on the m_{inv} dependence of the CME as well as magnetic field calculations will be helpful to improve this upper limit in the future.

[1] T. D. Lee and G. C. Wick, Vacuum stability and vacuum excitation in a spin-0 field theory, Phys. Rev. D **9**, 2291 (1974).

[2] D. Kharzeev, R. D. Pisarski, and M. H. G. Tytgat, Possibility of Spontaneous Parity Violation in Hot QCD, Phys. Rev. Lett. **81**, 512 (1998).

[3] D. Kharzeev and R. D. Pisarski, Pionic measures of parity and CP violation in high-energy nuclear collisions, Phys. Rev. D **61**, 111901(R) (2000).

[4] K. Fukushima, D. E. Kharzeev, and H. J. Warringa, Chiral magnetic effect, Phys. Rev. D **78**, 074033 (2008).

[5] B. Müller and A. Schafer, Charge fluctuations from the chiral magnetic effect in nuclear collisions, Phys. Rev. C **82**, 057902 (2010).

[6] D. E. Kharzeev, L. D. McLerran, and H. J. Warringa, The effects of topological charge change in heavy ion collisions: "Event by event $\mathcal{P}$ and $\mathcal{CP}$ violation," Nucl. Phys. A **803**, 227 (2008).

[7] M. Asakawa, A. Majumder, and B. Muller, Electric charge separation in strong transient magnetic fields, Phys. Rev. C **81**, 064912 (2010).

[8] D. E. Kharzeev and H. J. Warringa, Chiral magnetic conductivity, Phys. Rev. D **80**, 034028 (2009).

[9] K. Tuchin, Time and space dependence of the electromagnetic field in relativistic heavy-ion collisions, Phys. Rev. C **88**, 024911 (2013).

[10] D. Kharzeev, Parity violation in hot QCD: Why it can happen, and how to look for it, Phys. Lett. B **633**, 260 (2006).

[11] S. Shi, Y. Jiang, E. Lilleskov, and J. Liao, Anomalous chiral transport in heavy ion collisions from anomalous-viscous fluid dynamics, Ann. Phys. **394**, 50 (2018).

[12] D. E. Kharzeev, J. Liao, S. A. Voloshin, and G. Wang, Chiral magnetic and vortical effects in high-energy nuclear collisions—A status report, Prog. Part. Nucl. Phys. **88**, 1 (2016).

[13] J. Zhao, Search for the chiral magnetic effect in relativistic heavy-ion collisions, Int. J. Mod. Phys. A **33**, 1830010 (2018).

[14] J. Zhao, Z. Tu, and F. Wang, Status of the chiral magnetic effect search in relativistic heavy-ion collisions, Nucl. Phys. Rev. **35**, 225 (2018).

[15] J. Zhao and F. Wang, Experimental searches for the chiral magnetic effect in heavy-ion collisions, Prog. Part. Nucl. Phys. **107**, 200 (2019).

[16] W. Li and G. Wang, Chiral magnetic effects in nuclear collisions, Ann. Rev. Nucl. Part. Sci. **70**, 293 (2020).

[17] A. M. Sirunyan *et al.*, Constraints on the chiral magnetic effect using charge-dependent azimuthal correlations in *p*Pb and PbPb collisions at the CERN Large Hadron Collider, Phys. Rev. C **97**, 044912 (2018).

[18] S. Acharya *et al.*, Constraining the magnitude of the chiral magnetic effect with event shape engineering in Pb-Pb collisions at $\sqrt{s_{NN}} = 2.76$ TeV, Phys. Lett. B **777**, 151 (2018).

[19] H.-J. Xu, J. Zhao, X. Wang, H. Li, Z.-W. Lin, C. Shen, and F. Wang, Varying the chiral magnetic effect relative to flow in a single nucleus-nucleus collision, Chin. Phys. C **42**, 084103 (2018).

[20] A. H. Tang, Probe chiral magnetic effect with signed balance function, Chin. Phys. C **44**, 054101 (2020).

[21] V. Koch, S. Schlichting, V. Skokov, P. Sorensen, J. Thomas, S. Voloshin, G. Wang, and H.-U. Yee, Status of the chiral magnetic effect and collisions of isobars, Chin. Phys. C **41**, 072001 (2017).

[22] M. Abdallah *et al.*, Search for the chiral magnetic effect with isobar collisions at $\sqrt{s_{NN}} = 200$ GeV by the STAR Collaboration at RHIC, Phys. Rev. C **105**, 014901 (2022).

[23] B. Alver *et al.*, System Size, Energy, Pseudorapidity, and Centrality Dependence of Elliptic Flow, Phys. Rev. Lett. **98**, 242302 (2007).

[24] S. A. Voloshin, Parity violation in hot QCD: How to detect it, Phys. Rev. C **70**, 057901 (2004).

[25] B. I. Abelev *et al.*, Observation of charge-dependent azimuthal correlations and possible local strong parity violation in heavy ion collisions, Phys. Rev. C **81**, 054908 (2010).

[26] B. I. Abelev *et al.*, Azimuthal Charged-Particle Correlations and Possible Local Strong Parity Violation, Phys. Rev. Lett. **103**, 251601 (2009).

[27] F. Wang and J. Zhao, Challenges in flow background removal in search for the chiral magnetic effect, Phys. Rev. C **95**, 051901(R) (2017).

[28] S. Schlichting and S. Pratt, Charge conservation at energies available at the BNL Relativistic Heavy Ion Collider and contributions to local parity violation observables, Phys. Rev. C **83**, 014913 (2011).

[29] A. Bzdak, V. Koch, and J. Liao, Azimuthal correlations from transverse momentum conservation and possible local parity violation, Phys. Rev. C **83**, 014905 (2011).

[30] B. Müller, Looking for parity violation in heavy-ion collisions, Physics **2**, 104 (2009).

[31] L. Adamczyk *et al.*, Beam-Energy Dependence of Charge Separation along the Magnetic Field in Au + Au Collisions at RHIC, Phys. Rev. Lett. **113**, 052302 (2014).

[32] B. Abelev *et al.*, Charge Separation Relative to the Reaction Plane in Pb-Pb Collisions at $\sqrt{s_{NN}} = 2.76$ TeV, Phys. Rev. Lett. **110**, 012301 (2013).

[33] V. Khachatryan *et al.*, Observation of Charge-Dependent Azimuthal Correlations in *p*-Pb Collisions and Its Implication for the Search for the Chiral Magnetic Effect, Phys. Rev. Lett. **118**, 122301 (2017).

[34] F. Wang, Effects of cluster particle correlations on local parity violation observables, Phys. Rev. C **81**, 064902 (2010).

[35] A. Bzdak, V. Koch, and J. Liao, Remarks on possible local parity violation in heavy ion collisions, Phys. Rev. C **81**, 031901(R) (2010).

[36] S. Pratt, S. Schlichting, and S. Gavin, Effects of momentum conservation and flow on angular correlations at RHIC, Phys. Rev. C **84**, 024909 (2011).

[37] L. Adamczyk *et al.*, Measurement of charge multiplicity asymmetry correlations in high-energy nucleus-nucleus collisions at $\sqrt{s_{NN}} = 200$ GeV, Phys. Rev. C **89**, 044908 (2014).

[38] J. Zhao, Y. Feng, H. Li, and F. Wang, HIJING can describe the anisotropy-scaled charge-dependent correlations at the BNL Relativistic Heavy Ion Collider, Phys. Rev. C **101**, 034912 (2020).

[39] J. Adam *et al.*, Charge-dependent pair correlations relative to a third particle in *p* + Au and *d* + Au collisions at RHIC, Phys. Lett. B **798**, 134975 (2019).

[40] J. Schukraft, A. Timmins, and S. A. Voloshin, Ultra-relativistic nuclear collisions: Event shape engineering, Phys. Lett. B **719**, 394 (2013).

[41] V. Toneev and V. Voronyuk, Energy and system-size dependence of the chiral magnetic effect, EPJ Web Conf. **13**, 02005 (2011).

[42] B.-X. Chen and S.-Q. Feng, A systematical study of the chiral magnetic effects at the RHIC and LHC energies, Chin. Phys. C **44**, 024104 (2020).

[43] K. H. Ackermann, Jr. *et al.*, STAR detector overview, Nucl. Instrum. Methods Phys. Res., Sect. A **499**, 624 (2003).

[44] M. Anderson *et al.*, The Star time projection chamber: A unique tool for studying high multiplicity events at RHIC, Nucl. Instrum. Methods Phys. Res., Sect. A **499**, 659 (2003).

[45] K. H. Ackermann *et al.*, The STAR time projection chamber, Nucl. Phys. A **661**, 681 (1999).

[46] W. J. Llope, Multigap RPCs in the STAR experiment at RHIC, Nucl. Instrum. Methods Phys. Res., Sect. A **661**, S110 (2012).

[47] L. Adamczyk *et al.*, Inclusive charged hadron elliptic flow in Au + Au collisions at $\sqrt{s_{NN}} = 7.7$–39 GeV, Phys. Rev. C **86**, 054908 (2012).

[48] N. Borghini, P. M. Dinh, and J. Y. Ollitrault, Analysis of directed flow from elliptic flow, Phys. Rev. C **66**, 014905 (2002).

[49] L. Adamczyk *et al.*, Elliptic flow of identified hadrons in Au + Au collisions at $\sqrt{s_{NN}}$ = 7.7–62.4 GeV, Phys. Rev. C **88**, 014902 (2013).

[50] J. Adams *et al.*, ρ^0 Production and Possible Modification in Au + Au and $p + p$ Collisions at $\sqrt{s_{NN}}$ = 200 GeV, Phys. Rev. Lett. **92**, 092301 (2004).

[51] J. Zhao, H. Li, and F. Wang, Isolating the chiral magnetic effect from backgrounds by pair invariant mass, Eur. Phys. J. C **79**, 168 (2019).

[52] F. Wen, J. Bryon, L. Wen, and G. Wang, Event-shape-engineering study of charge separation in heavy-ion collisions, Chin. Phys. C **42**, 014001 (2018).

[53] A. Bzdak and V. Skokov, Event-by-event fluctuations of magnetic and electric fields in heavy ion collisions, Phys. Lett. B **710**, 171 (2012).

[54] R. Belmont and J. L. Nagle, To CME or not to CME? Implications of $p + $ Pb measurements of the chiral magnetic effect in heavy ion collisions, Phys. Rev. C **96**, 024901 (2017).

[55] Y. Sun, Y. Wang, Q. Li, and F. Wang, Effect of internal magnetic field on collective flow in heavy ion collisions at intermediate energies, Phys. Rev. C **99**, 064607 (2019).

[56] H. Li, J. Zhao, and F. Wang, A novel invariant mass method to isolate resonance backgrounds from the chiral magnetic effect, Nucl. Phys. A **982**, 563 (2019).

[57] G. J. Feldman and R. D. Cousins, A Unified approach to the classical statistical analysis of small signals, Phys. Rev. D **57**, 3873 (1998).

[58] M. S. Abdallah *et al.*, Search for the chiral magnetic effect via charge-dependent azimuthal correlations relative to spectator and participant planes in Au + Au collisions at $\sqrt{s_{NN}}$ = 200 GeV, Phys. Rev. Lett. **128**, 092301 (2022).